RZ 3832 (# Z1209-001) 09/10/2012
Electrical Engineering 7 pages

Research Report

Design and fabrication of micro-cantilevers for multi-frequency atomic force microscopy

Abu Sebastian,[1] Naveen Shamsudhin,[1,a)] Hugo Rothuizen,[1] Ute Drechsler,[1] Wabe W. Koelmans,[2] Harish Bhaskaran,[1,b)] Hans Joachim Quenzer,[3] Bernhard Wagner,[3] and Michel Despont[1]

[1]IBM Research – Zurich, 803 Rüschlikon, Switzerland

[2]MESA+ Institute for Nanotechnology, University of Twente, PO Box 217, 7500 AE Enschede, The Netherlands

[3]Fraunhofer Institut für Siliziumtechnologie, 25524 Itzehoe, Germany

a) Naveen Shamshudin is currently at Institute of Robotics and Intelligent Systems, ETH Zurich, 8092 Zurich, Switzerland

b) Harish Bhaskaran is currently at College of Engineering, Mathematics and Physical Sciences, University of Exeter, Devon EX4 4QF, England

Design and fabrication of micro-cantilevers for multi-frequency atomic force microscopy

Abu Sebastian,[1] Naveen Shamsudhin,[1, a)] Hugo Rothuizen,[1] Ute Drechsler,[1] Wabe W. Koelmans,[2] Harish Bhaskaran,[1, b)] Hans Joachim Quenzer,[3] Bernhard Wagner,[3] and Michel Despont[1]

[1)]*IBM Research-Zurich, CH-8803 Rüschlikon, Switzerland.*

[2)]*MESA$^+$ Institute for Nanotechnology, University of Twente, PO Box 217, NL-7500 AE Enschede, The Netherlands*

[3)]*Fraunhofer Institut für Siliziumtechnologie, D-25524 Itzehoe, Germany*

(Dated: 7 September 2012)

Several multi-frequency operation modes have recently been proposed that exhibit significant promise in terms of their ability to discern various material properties. In this article, we report the design, fabrication and characterization of cantilevers with integrated actuation and conductive probes for multi-frequency atomic force microscopy (AFM). The cantilevers are equipped with aluminum nitride piezoelectric actuators and platinum silicide tips. The integrated actuation results in a significantly improved dynamic behavior as compared to the use of external piezo-actuators. The platinum silicide tips provide excellent electrical sensing capability. These cantilevers also possess a stepped-rectangular geometry that ensures that the resonance frequencies corresponding to the first four normal bending modes fall within a frequency range of 1 MHz. The dynamic behavior of these cantilevers is explored using both finite element simulations and experimental methods. These cantilevers exhibit excellent dynamic behavior over a wide frequency range, both off-contact and on-contact with a sample. Imaging experiments utilizing higher eigenmodes as well as bimodal imaging are presented. Also shown is the use of these cantilevers for normal force modulation for enhanced electrical sensing capability.

I. INTRODUCTION

Since its invention in 1986, the atomic force microscope (AFM) has been one of the quintessential instruments for nanoscale science and engineering. The AFM is used not only to view, but also to create and manipulate nanoscale features on or below the sample surface. The tip-sample interaction force is sensed by a micro-cantilever, and in this way, local surface properties can be mapped with nanoscale spatial resolution. These microscopes are used in a variety of application areas, such as life sciences[1,2], semiconductor metrology[3], nanofabrication,[4,5] data storage[6] and material science[7,8].

The traditional modes of AFM operation, such as the contact and the dynamic mode, have inherent limitations in terms of their ability to measure tip-sample interaction forces as well as in terms of the achievable bandwidth and resolution. However, in recent years, several multi-frequency modes of operation have been proposed that show significant promise in terms of their ability to investigate various material properties[9,10]. These modes of operation involve the excitation and detection of one or more of the resonance frequencies usually associated with the various eigenmodes of the cantilever while it is freely oscillating or in-contact with the sample. They usually are collectively referred to as multi-frequency AFM (MF-AFM). Examples include higher-harmonic imaging, where the cantilever is typically actuated at the first resonance frequency and the higher harmonics of this oscillation frequency generated by the nonlinear tip-sample interaction force are monitored[11]. The use of higher resonance frequencies could speed up the settling time in amplitude-modulation AFM[12]. Bi-modal AFM, where the microcantilever is driven at two different eigenfrequencies simultaneously[13,14], has been successfully used to image antibodies in air and liquid[15] and to detect modal vibrations in graphene and multiwalled carbon nanotubes[16,17]. Contact-resonance imaging and band excitation techniques also show tremendous potential in terms of their ability to discern material properties[18,19]. Actuation at the contact resonance frequencies also results in reduced friction and enhanced electrical contact quality[20,21].

In spite of the tremendous promise of MF-AFM, deciphering and exploiting the complicated dynamics involved when a multi-modal cantilever interacts with the nonlinear tip-sample interaction force remains a key challenge. A significant step towards addressing this challenge is the design of special-purpose cantilevers for MF-AFM. In this article, we present the design, fabrication and characterization of micro-cantilevers with integrated actuation and conductive tips that are particularly well suited for MF-AFM.

For quantitative MF-AFM, it is almost essential to have a well-defined dynamic behavior of the actuator-cantilever system, including the phase response over a wide bandwidth. This potentially facilitates the application of powerful tools such as harmonic balance from the theory of dynamical systems for deciphering tip-sample interaction forces. One way to achieve well-defined dynamic behavior is by integrating piezo-electric actuators on the cantilever. Various piezoelectric materials such as zinc oxide (ZnO) and lead zirconium titanate (PZT) have been used to develop integrated actuators for micro-cantilevers[22,23]. In the cantilevers presented here, aluminium nitride (AlN) is used as the piezoelectric material.

[a)]currently at Institute of Robotics and Intelligent Systems, ETH Zurich, 8092 Switzerland

[b)]currently at College of Engineering, Mathematics and Physical Sciences, University of Exeter, Devon EX4 4QF, England

AlN integration has the advantage of full-CMOS compatibility, is amenable to dry-etch patterning, has long-term piezoelectric stability, and exhibits very low nonlinear effects such as hysteresis and creep[24]. For MF-AFM we also believe it is advantageous to reduce the spacing between the resonance frequencies. The closely spaced resonance frequencies could enhance the various higher harmonics being generated via the tip-sample interaction forces. Moreover, this way the higher resonance frequencies will be more accessible to the sensing and actuation electronics. In conventional rectangular cantilevers, there is a wide separation between the resonance frequencies corresponding to the different eigenmodes. The cantilevers presented in this article possess stepped rectangular geometries to reduce the spacing between the resonance frequencies along the lines of the approach presented by Sadewasser et al.[25].

MF-AFM has also been shown to be suitable for mapping magnetic and electrical properties[26,27]. The mapping of electrical properties is particularly attractive for semiconductor metrology and the exploration of nanoscale electronic devices[28]. The cantilevers described here are integrated with recently developed platinum-silicide probe technology[29]. These tips can sustain high currents while maintaining nanoscale-sharp tip apices. These cantilevers could serve as powerful experimental tools in quantitative MF-AFM applications in nanoscale electrical sensing[30].

The remainder of the article is structured as follows. In Section II, the design and fabrication of the cantilevers is presented. Section III contains the finite element simulations and Section IV the experimental identification of the cantilever dynamics. Finally in Section V, the efficacy of these cantilevers is illustrated through several imaging experiments.

II. DESIGN AND FABRICATION

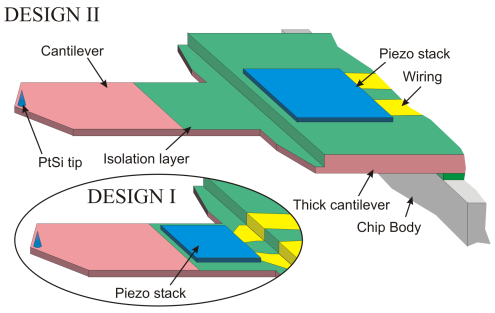

FIG. 1. Schematic of the cantilever designs. The primary difference between the two cantilever designs is in the physical location of the actuator.

Figure 1 shows a schematic of the fabricated cantilever with integrated actuator and conducting tip. The cantilever has a stepped rectangular geometry with two rectangular segments, a wider and thicker section (220 μm long, 130 μm wide and 4μm thick) combined with a narrower and thinner section (100 μm long, 30 μm wide and 1.5 μm thick). The cantilever tip is approximately 2 μm tall. The cantilevers are fabricated with the piezoelectric stack attached to different regions of the cantilever. In this article, we present cantilevers with two types of actuator placement. In one design, the actuator is placed on the narrow and thin section of the cantilever (denoted design I). In the other design, the actuator is placed on the thick wide upper section of the cantilever (denoted design II). As we will see later, the dynamic behavior of these two designs differ significantly owing to the placement of the actuator. Cantilever fabrication is based on the silicon-on-insulator (SOI) cantilever platform, isotropic Reactive Ion Etching (RIE) of the tip, and deep RIE to structure the chip body. The cantilever is made of highly doped silicon, a requirement for conducting-mode operation. On the tip itself, a platinum silicide (PtSi) layer is formed[29]. A contact pad on the device layer of the SOI wafer allows a potential to be applied to the tip (not shown in Fig. 1). The piezoelectric actuator is composed of an AlN layer. AlN is chosen because of its wide appeal in micro-electro-mechanical systems and semiconductor fabrication. Furthermore, AlN is known to have less creep and no hysteresis, which ensures linear dynamic behavior for the cantilevers. Compared to PZT, AlN is also lead free and does not need extra poling. To electrically decouple the conductive tip from the piezoelectric actuator, a dielectric isolation layer of SiO_2 is introduced.

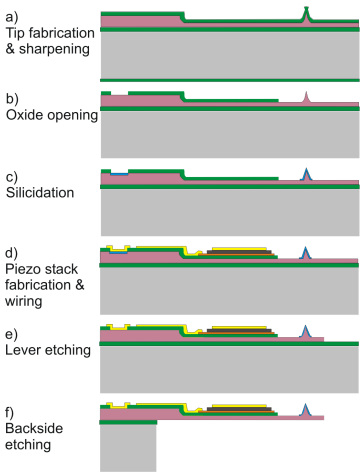

FIG. 2. Schematic illustrating the process flow of cantilever fabrication.

Figure 2 describes the process used to fabricate these cantilevers. The starting substrate is a 4 inch SOI wafer with a 3.5-μm-thick, epitaxially grown silicon membrane and a 0.4-μm-thick buried oxide (BOX). The membrane is n-doped with phosphorous at a concentration of 10^{18} at/cm^3, which limits the serial resistance in conduction mode. The first step consists of thermally growing a 500 nm layer of oxide, which is used as mask material when etching the thick anchor legs and the tip. CHF_3/O_2-based RIE is used to open this oxide, followed by an isotropic SF_6/Ar RIE process to etch an hourglass-shaped precursor of the tip into the membrane (Fig. 2(a)). The oxide mask is then removed and an oxidation sharpening technique is used to finalize the tip shape. After

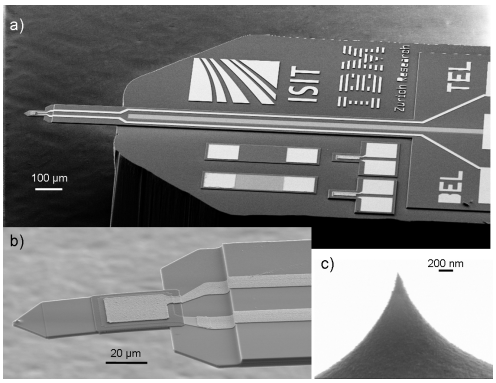

FIG. 3. Scanning electron micrographs (SEM) of the fabricated cantilever (design I). (a) SEM of the entire chip. The three electrical contacts on the right are for the actuators (TEL and BEL) and for the tip (middle one). (b) View of the cantilever. (c) Detail of the PtSi tip apex.

being patterned by buffered hydroflouric acid (BHF), this oxide will be used as isolation layer (Fig. 2(b)). By lift-off of 50 nm of platinum, followed by annealing to form the PtSi, the tip as well as the contact to the silicon are converted to a silicide. The Pt not consumed by the silicidation process is then selectively etched (Fig. 2(c)). This technique reliably yields tips with apex radii below 10 nm. The piezoelectric stack fabrication starts by the bottom electrode consisting of a Pt/Ti (100 nm/10 nm) layer patterned by lift-off technique. It is followed by the deposition of a 500 nm thick AlN layer deposited by sputtering. A Molybdenum layer is used subsequently as a hard mask for the wet etching of the AlN in hot tetramethylammonium hydroxide (TMAH) solution before to be removed. A lift-off of 500 nm gold, which has been deposited by sputtering, is done for fabrication of the top electrode, the wiring and the contacts (including the one contacting silicon) as shown in Fig. 2(d). The front-side process is finalized by the transfer of the cantilever shape into the remaining Si membrane using RIE and the buried SOI oxide as an etch stop (Fig. 2(e)). Finally, after protecting the front side with a resist layer, the chip body itself is structured using deep RIE and the cantilever is released after the etching of the buried oxide with BHF and front-side resist stripping (Fig. 2(f)). Scanning electron micrograph (SEM) of the finished cantilever are shown in Fig. 3.

III. FINITE-ELEMENT MODELING

To gain insights into the dynamics of these cantilevers, electro-mechanical finite-element simulations were performed using software tools from ANSYS (*ANSYS Multiphysics, ANSYS Inc., Canonsburg PA*). The AlN region was meshed using coupled-field solid elements (SOLID226) to model the piezoelectric actuation. For the other structural-domain-only regions of the lever, we employed a hybrid solid-shell element (SOLSH190) appropriate for thin and layered geometries. The dominant structural material is Silicon, for

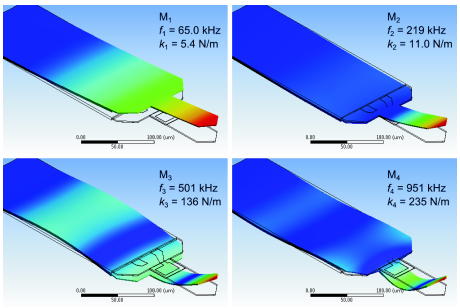

FIG. 4. Illustration of the first four bending modes of the microcantilever. The resonance frequencies and the stiffness values associated with the transverse bending modes are also indicated.

which we used a Young's Modulus of 169 GPa, and a Poisson's Ratio of 0.22. The frequency response (actuation transfer function) for a given lever geometry was derived by modal superposition, subsequent to a modal analysis which yielded the eigenmode shapes as well as the structural load vector resulting from a voltage applied across the actuator patch. Examples of the calculated transfer function are shown in the next section, in comparison with experimental measurement.

The input quantity for the transfer function is the applied actuation voltage, and the output is the out-of-plane displacement averaged over a monitor patch representing the laser spot, located on the lever surface opposite the tip. To account for the finite size of the laser beam incident on the cantilever, the monitor spot is a 10 μm diameter disk, consistent with our calculations of the laser spot size of the optical sensing system.

Because the simulation results are sensitive to details of the cantilever geometry - in particular the thicknesses of the different lever regions - we used SEM measurements of the fabricated cantilever to ensure the parameters used in the simulation are accurately matched to those in experiments. Materials parameters used were standard from literature, with the exception of the piezoelectric coefficients of the AlN, which was initially set arbitrarily for the simulations, and then rescaled to obtain the same DC actuation gains as observed in the experiments. Similarly, modal damping coefficients used in the model, which have an impact only on the quality factor of the resonances, but not on the predicted eigenfrequencies, were adjusted for agreement with experiment (a proportional damping of 0.25% was found optimal for these levers when off-contact).

When off-contact, the cantilever system has clamped-free boundary conditions, i.e., one end is free to move and rotate whereas the other end is not. These boundary conditions determine the physical shapes of the discrete transverse eigenmodes of the system. The first four transverse modal shapes of the stepped cantilever obtained through finite-element simulations are shown in Fig. 4. This figure illustrates the contributions of the individual segments of the lever to its overall bending. We refer to the individual eigenmodes as M_1, M_2, M_3 and M_4 for brevity of notation. For M_1, both rectangular segments contribute to the mode shape, whereas for the higher modes, the deflection at the tip originates mainly with the bending of

the smaller rectangular segment. Thus the frequency spacing between M_1 and the higher modes, which would be fixed in the case of a single-segment simple rectangular-beam lever, may in this case be tuned by controlling the relative stiffness of the two different sections of the lever.

IV. EXPERIMENTAL IDENTIFICATION

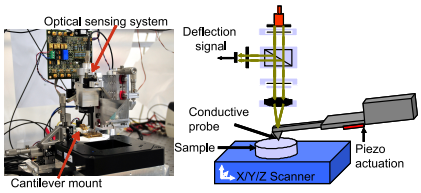

FIG. 5. Experimental setup. The primary components are a nanopositioning stage with $X/Y/Z$ motion capability, the cantilever-sample system and an optical deflection sensing system. (a) Photograph. (b) Schematic.

A custom-made AFM is used for the experimental identification of the cantilever dynamics and the imaging experiments. The AFM consists of a nanopositioning stage with $X/Y/Z$ motion capability and the sample holder, the cantilever and its mount, an optical sensing subsystem, and the electronic data-acquisition and control units (see Fig. 5). Furthermore a DSP/FPGA board and a computer are used for controlling the experiment and for image postprocessing and display. The optical sensing system operates on the beam deflection principle and hence measures the angular changes of the cantilever as opposed to the true deflection of the cantilever. Note that this is accounted for in the finite-element simulations.

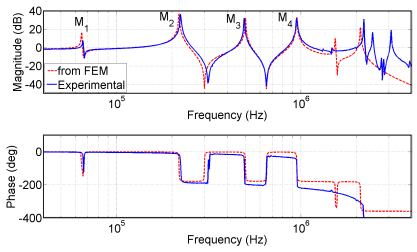

FIG. 6. Match between the experimentally identified frequency response and the one obtained through finite-element simulations.

To characterize these cantilevers, we used an HF2LI lock-in amplifier from *Zurich Instruments*. To obtain the piezo excitation transfer function, we actuated the AlN actuator with a swept sine wave from 40 kHz till 4 MHz. The transfer function relating the photodiode signal to the actuation signal is obtained. The frequency response corresponding to cantilever design I is shown in Fig. 6. There is an excellent match between this and the one obtained via finite-element simulations. The resonance frequencies corresponding to the first four normal modes are clearly visible. The close-packing of the

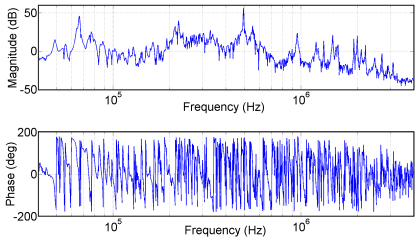

FIG. 7. Cantilever frequency response obtained using an external dither piezo-electric actuator.

resonance frequencies is due to the unconventional stepped-rectangular geometry. The classic ω_2/ω_1 ratio of 6.267 for rectangular cantilevers is no longer valid for these cantilevers, with the second mode being closer in frequency at a ω_2/ω_1 ratio of 3.368. The existence of four resonance frequencies in a frequency range of 1 MHz makes them particularly well suitable for higher-mode, higher-harmonic and multi-modal imaging techniques. The higher harmonics generated by nonlinear tip-sample interaction typically get filtered out when the spacing between the frequencies is large as in the case of a rectangular cantilever[31]. The cantilever acts as a mechanical filter and inherently limits the ability to discern tip-sample interaction forces. On the other hand, if the resonance frequencies are more closed spaced, then they could potentially amplify the higher-harmonics being generated thus enhancing the coupling between the tip-sample interaction forces and the sensor, which is the cantilever. Yet another advantage is to have the various resonance frequencies accessible to the sensing and signal processing circuitry.

The experimental frequency response also illustrates the lack of spurious modes and the cleanliness of the phase response over a wide frequency range as predicted in the finite-element model. This is attributed to the integrated piezoelectric actuators. To illustrate the difference in the dynamic behavior, a similar dynamical response of the same cantilever is obtained using an externally mounted dither piezo (see Fig. 7). Even though there is substantial cantilever motion when actuated at the various resonance frequencies, the overall dynamic response is significantly inferior to the one obtained through integrated actuation. The response obtained while using external piezo-actuation is probably worsened by the inferior coupling of the external piezo-actuator with the specific cantilever base structure. However, even with better coupling, it is almost impossible to achieve such a clean frequency response over a MHz bandwidth.

Such well-defined dynamic behavior is a significant step towards quantitative MF-AFM. Given the complexity of the dynamics involved, it is essential that one resorts to the theory of dynamic systems for the analysis and design of MF-AFM techniques. Such approaches have already been employed for the analysis of dynamic-mode AFM[31–33]. Equipped with an accurate description of the cantilever dynamics, one can resort to powerful techniques such as harmonic balance to reconstruct the tip-sample interaction forces.

The frequency response corresponding to cantilever design

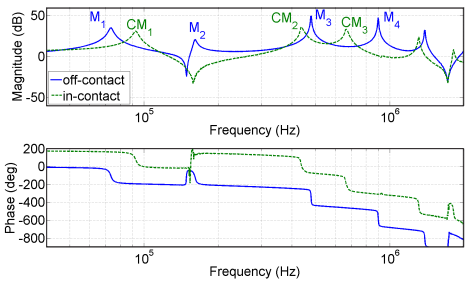

FIG. 8. Cantilever frequency response while off-contact and in contact with the sample surface.

II is shown in Fig. 8. The positioning of the actuator on this cantilever suppresses the motion of mode M_2 by essentially not allowing the the beam to flex in the corresponding modal shape. The actuator placement is also responsible for the partial suppression of mode M_1 in cantilever design I. Although both types of cantilevers exhibit the same modal shapes, the expression of particular modal shapes can be suppressed by suitable positioning of the actuators. Another key difference can be seen in the phase response. Cantilever design I exhibits collocated dynamics over a MHz range whereas cantilever design II exhibits non-collocated dynamics characteristic of a series configuration of harmonic oscillators. This ability to tune the dynamic behavior by merely changing the position of the actuator could be very advantages for the design of MF-AFM techniques.

Figure 8 also shows the frequency response obtained while in contact with the sample surface: These cantilevers exhibit excellent dynamic behavior while in contact with the sample surface as well. This is highly advantageous for imaging at the contact resonance modes as well as normal force modulation for enhanced electrical sensing, as will be illustrated in the next section.

V. IMAGING RESULTS

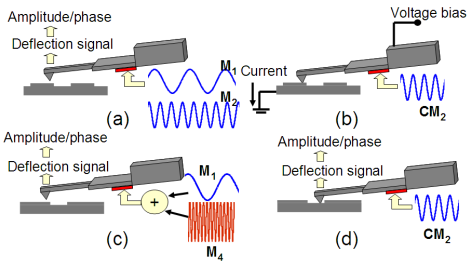

FIG. 9. Schematics of the AFM modes presented in this article. (a) Amplitude-modulation AFM with various off-contact bending modes. (b) Force modulation for enhanced electrical sensing. (c) Bimodal AFM. (d) Amplitude-modulation AFM with in-contact bending modes.

In the previous sections, we presented the design, fabrication, finite element modeling and experimental identification of the cantilevers. In this section, we present a variety of experiments to illustrate the applicability of these cantilevers for a variety of state-of-the-art AFM modes. These experiments are intended to demonstrate the functionality and versatility of these cantilevers. A schematic of the various AFM modes is presented in Fig. 9.

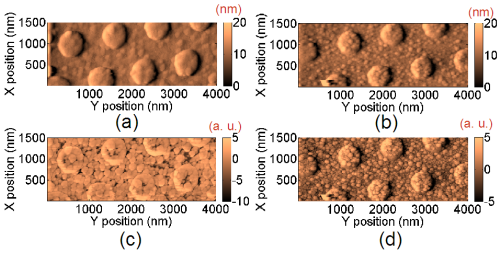

FIG. 10. Amplitude-modulation AFM imaging using two normal modes. Map of amplitude signal variations corresponding (a) to M_1 (b) to M_2 and phase signal variations corresponding (c) to M_1 (d) to M_2.

First we show the applicability of these cantilevers for amplitude-modulation AFM (AM-AFM) using multiple off-contact modes. In this mode of operation, the cantilever interacts intermittently with the sample. In spite of a few demonstrations of AM-AFM at higher resonances, the most notable result to date has been the operation of an AM-AFM achieved by exciting the second cantilever resonance under ultrahigh vacuum[12]. Accessibility of the higher resonance frequencies by the signal processing circuitry as well as stability of the corresponding periodic orbits are key challenges. Using the cantilevers presented in this paper, it was possible to obtain stable periodic orbits using M_1 and M_2 of the cantilever with significant tip-sample interaction in ambient conditions. Moreover, the second resonance frequencies are easily accessible to the sensing and signal processing electronics. The sample consists of 20 nm thick platinum pads evaporated on a stack of tungsten and tetrahedral amorphous carbon (t-aC). In Fig. 10, the amplitude and phase images while imaging in constant-height mode in amplitude-modulation AFM is shown. The higher resolution of imaging with M_2 is attributed to the higher quality factor.

Next we present an experiment that simultaneously demonstrates the electrical sensing capability as well as actuation capability at higher contact resonant modes. We present a novel concept of using normal force modulation for enhanced electrical contact quality. This concept was first illustrated using rectangular conductive-AFM cantilevers utilizing the first contact resonant frequency[21]. The essential idea is to oscillate the cantilever with a small oscillation amplitude, preferably at one of the contact resonance frequencies, during conductive-mode AFM imaging. This normal force modulation that acts on top of the DC loading force results in reduced friction and wear, and, more importantly, enhanced electrical sensing capability. An experiment was performed using cantilever design I and the sample with platinum pads. The imaging results are presented in Fig. 11. Figures 11(a) and (b) show

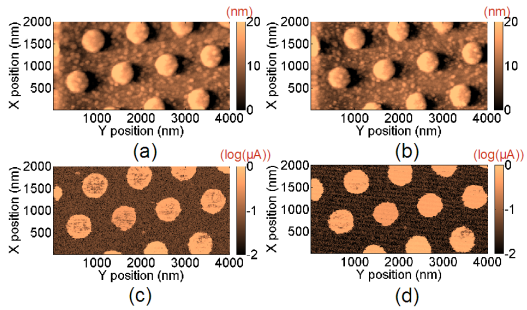

FIG. 11. Simultaneous topography and electrical sensing with and without normal force modulation. Map of the variations in (a) deflection signal (without normal force modulation), (b) deflection signal (with force modulation), (c) current signal (without force modulation), and (d) current signal (with force modulation).

the images obtained using the deflection signal while the tip is scanned across the sample in constant-height mode. In Fig. 11 (a), the cantilever is not oscillated, whereas in Fig. 11 (b), it is oscillated at its second in-contact resonance frequency. The corresponding current maps are shown in Figures 11 (c) and 11 (d), respectively. There is no perceivable change in the topography maps, whereas the current map shows a significantly better electrical contact quality with normal force modulation.

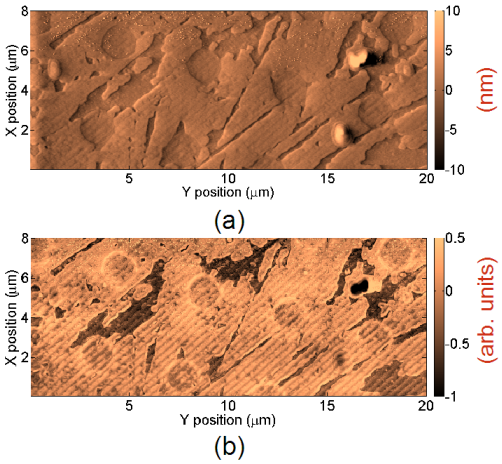

FIG. 12. Bimodal imaging. Map of the amplitude signal variations corresponding (a) to M_1 and (b)to M_4. The lighter shade corresponds to Ti.

Next we illustrate the usefulness of the newly designed cantilevers for bimodal AFM imaging. Demonstrations of bimodal imaging using standard cantilevers are almost always utilizing the first and second modes. Here we illustrate bimodal imaging by actuating the cantilever (design II) simultaneously in M_1 and M_4. Note that in these cantilevers, even the fourth mode well accessible to the sensing and signal processing modules. The motion in M_1 is chosen to be substantially bigger than that in M_4. To demonstrate the applicability of this mode of operation to resolve material properties, a sample is chosen that consists of a silicon surface with irregular regions of titanium. Chemical mechanical polishing is performed to reduce the topographical variations. The images created using the amplitude signals corresponding to M_1 and M_4 are shown in Fig. 12. The oscillation amplitude corresponding to M_1 is chosen to be approx. 90 nm and hence is much larger than the topographical variations on the sample. While the amplitude signal corresponding to M_1 provides the topography estimate, the amplitude signal corresponding to M_4 provides information on the underlying material. The regions with a distinctly lighter shade correspond to titanium.

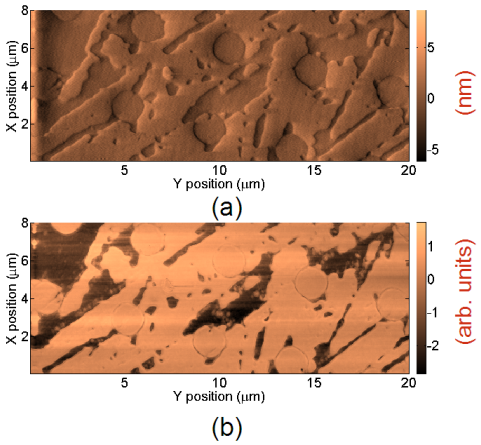

FIG. 13. Contact-resonance imaging. Map of the variations in (a) the mean deflection signal and (b) the amplitude signal corresponding to CM_2.

An alternative to distinguish material contrast is by contact-resonance imaging. This mode of operation is similar to normal force modulation for electrical sensing, but, the amplitude of the cantilever oscillation when actuated at one of the contact resonance frequencies is monitored while the cantilever is scanned across the sample surface in constant-height mode. Owing to the changes in the local material stiffness, there will be a change in the contact resonance frequencies. As the cantilever is driven at a constant frequency, such a change will translate into a change in the oscillation amplitude. The low-pass-filtered deflection signal, on the other hand, should be a good measure of the topographical variations as in regular contact-mode AFM. In the experiment presented here, again the second contact resonant mode is utilized. In Fig. 13(a), the image obtained using the filtered deflection signal is shown. This corresponds to the topography map. In Fig. 13(b), the image obtained using the amplitude signal is shown. This image clearly shows the material contrast.

The experiments presented in this section illustrate the applicability of the cantilevers described herein for a variety of state-of-the-art AFM modes of operation that involve sensing of sample properties such as topography, visco-elastic properties and electric properties.

VI. CONCLUSIONS

Recently, several new multi-frequency operation modes have been proposed for AFM that show tremendous promise in terms of their ability to discern material properties. The operation modes involve the excitation and detection of one or more resonance frequencies associated with the higher eigenmodes of cantilevers while they are freely oscillating or in contact with the sample surface. A significant first step towards deciphering and exploiting the complicated dynamics that arises from these multi-frequency AFM modes is the design of a cantilever with excellent dynamic behavior, closely-spaced resonances and electrical sensing capability. Such cantilevers could serve as powerful experimental tools for quantitative MF-AFM. In this paper, we report the design, fabrication and characterization of cantilevers with integrated AlN piezo-electric actuators, an unconventional cantilever geometry, and PtSi conductive tips. Finite-element analysis and experimental measurements reveal the excellent dynamic behavior exhibited by these cantilevers over a wide frequency range. The excellent dynamic behavior will enable the use of system-theoretic approaches such as harmonic balance to decipher tip sample interaction forces. The dynamic behavior can also be tuned by the placement of the actuator. Because of the stepped-rectangular geometry of the cantilevers, the resonance frequencies corresponding to the first four normal modes appear within 1 MHz bandwidth. The closely spaced resonances could help address an inherent problem in AFM, that of the cantilever acting as a mechanical filter and filtering off the higher harmonics being generated through tip-sample interaction. These cantilevers also exhibit excellent dynamic behavior while in contact with the sample. Several experiments were performed to illustrate their applicability for several state-of-the-art AFM modes of operation, such as amplitude-modulation AFM using higher normal modes, bi-modal AFM using the first and fourth normal modes, normal force-modulation for enhanced electrical sensing and amplitude-modulation AFM using contact resonances.

ACKNOWLEDGMENTS

We would like to thank Laurent Dellman, Urs Egger and Walter Häberle for technical assistance, and Angeliki Pantazi, Tomas Tuma and John Lygeros for fruitful discussions. Special thanks to Haris Pozidis and Evangelos Eleftheriou for their support of this work. We would also like to thank Charlotte Bolliger for assistance with the preparation of this manuscript. We thank the European Research Council for financial support provided under an FP-6 grant for the project ProTeM Probe-based Terabit Memory FP6 Project 2005-IST-5-34719.

[1] M. Shibata, H. Yamashita, T. Uchihashi, H. Kandori, and T. Ando, Nature nanotechnology **5**, 208 (2010).
[2] M. Stolz, R. Gottardi, R. Raiteri, S. Miot, I. Martin, R. Imer, U. Staufer, A. Raducanu, M. Düggelin, W. Baschong, *et al.*, Nature Nanotechnology **5**, 821 (2010).
[3] A. Humphris, B. Zhao, D. Catto, J. Howard-Knight, P. Kohli, and J. Hobbs, Review of Scientific Instruments **82**, 043710 (2011).
[4] D. Pires, J. Hedrick, A. De Silva, J. Frommer, B. Gotsmann, H. Wolf, M. Despont, U. Duerig, and A. Knoll, Science **328**, 732 (2010).
[5] A. Tseng, Nano Today **6**, 493 (2011).
[6] A. Pantazi, A. Sebastian, T. Antonakopoulos, P. Bächtold, A. Bonaccio, J. Bonan, G. Cherubini, M. Despont, R. DiPietro, U. Drechsler, *et al.*, IBM Journal of Research and Development **52**, 493 (2008).
[7] J. Loos, Advanced Materials **17**, 1821 (2005).
[8] A. Sebastian, A. Pauza, C. Rossel, R. Shelby, A. Rodríguez, H. Pozidis, and E. Eleftheriou, New Journal of Physics **13**, 013020 (2011).
[9] R. García, *Amplitude Modulation Atomic Force Microscopy* (Wiley-VCH, 2010).
[10] R. Garcia and E. Herruzo, Nature Nanotechnology **7**, 217 (2012).
[11] J. Preiner, J. Tang, V. Pastushenko, and P. Hinterdorfer, Physical Review Letters **99**, 46102 (2007).
[12] P. Girard, M. Ramonda, and R. Arinero, Review of scientific instruments **77**, 096105 (2006).
[13] T. Rodríguez and R. García, Applied Physics Letters **84**, 449 (2004).
[14] R. Proksch, Applied Physics Letters **89**, 113121 (2006).
[15] S. Patil, N. Martinez, J. Lozano, and R. Garcia, Journal of Molecular Recognition **20**, 516 (2007).
[16] D. García-Sánchez, A. San Paulo, M. Esplandiú, F. Perez-Murano, L. Forró, A. Aguasca, and A. Bachtold, Physical Review Letters **99**, 85501 (2007).
[17] D. García-Sánchez, A. Van Der Zande, A. Paulo, B. Lassagne, P. McEuen, and A. Bachtold, Nano letters **8**, 1399 (2008).
[18] S. Jesse, S. Kalinin, R. Proksch, A. Baddorf, and B. Rodriguez, Nanotechnology **18**, 435503 (2007).
[19] J. P. Killgore, D. G. Yablon, A. H. Tsou, A. Gannepalli, P. A. Yuya, J. A. Turner, R. Proksch, and D. C. Hurley, Langmuir (2011).
[20] M. Lantz, D. Wiesmann, and B. Gotsmann, Nature Nanotechnology **4**, 586 (2009).
[21] W. Koelmans, A. Sebastian, L. Abelmann, M. Despont, and H. Pozidis, Nanotechnology **22**, 355706 (2011).
[22] B. Rogers, L. Manning, T. Sulchek, and J. Adams, Ultramicroscopy **100**, 267 (2004).
[23] Y. Miyahara, M. Deschler, T. Fujii, S. Watanabe, and H. Bleuler, Applied surface science **188**, 450 (2002).
[24] H. Quenzer, U. Drechsler, A. Sebastian, S. Marauska, B. Wagner, and M. Despont, Procedia Engineering **25**, 665 (2011).
[25] S. Sadewasser, G. Villanueva, and J. Plaza, Applied physics letters **89**, 033106 (2006).
[26] R. W. Stark, N. Naujoks, and A. Stemmer, Nanotechnology **18**, 065502 (2007).
[27] J. W. Li, J. P. Cleveland, and R. Proksch, Applied Physics Letters **94**, 163118 (2009).
[28] R. Oliver, Reports on Progress in Physics **71**, 076501 (2008).
[29] H. Bhaskaran, A. Sebastian, and M. Despont, IEEE Transactions on Nanotechnology **8**, 128 (2009).
[30] S. Magonov and J. Alexander, Microscopy and Microanalysis **17**, 587 (2011).
[31] A. Sebastian, M. Salapaka, D. Chen, and J. Cleveland, Journal of Applied Physics **89**, 6473 (2001).
[32] M. Stark, R. Stark, W. Heckl, and R. Guckenberger, Proceedings of the National Academy of Sciences **99**, 8473 (2002).
[33] A. Sebastian, A. Gannepalli, and M. Salapaka, Control Systems Technology, IEEE Transactions on **15**, 952 (2007).